CCFE
CULHAM CENTRE FOR FUSION ENERGY

UK Atomic Energy Authority

UKAEA-CCFE-PR(23)90

D. Kumar, J. Hargreaves, A. Bharj, A. Scorror, L. M. Harding, H. Dominguez-Andrade, R. Holmes, R. Burrows, H. Dawson, A. D. Warren, P.E.J. Flewitt, T.L. Martin

The Effects of Fusion Reactor Thermal Transients on the Microstructure of Eurofer-97 Steel

The Effects of Fusion Reactor Thermal Transients on the Microstructure of Eurofer-97 Steel

D. Kumar, J. Hargreaves, A. Bharj, A. Scorror, L. M. Harding, H. Dominguez-Andrade, R. Holmes, R. Burrows, H. Dawson, A. D. Warren, P.E.J. Flewitt, T.L. Martin

This is a preprint of a paper submitted for publication in Acta Materialia

The Effects of Fusion Reactor Thermal Transients on the Microstructure of Eurofer-97 Steel

D. Kumar[a*], J. Hargreaves[a], A. Bharj[a], A. Scorror[a], L. M. Harding[a], H. Dominguez-Andrade[a], R. Holmes[b], R. Burrows[b], H. Dawson[c], A. D. Warren[a], P.E.J. Flewitt[a], and T.L. Martin[a]

[a] *University of Bristol, H.H. Wills Physics Laboratory, Tyndall Avenue, Bristol, BS8 1TL, UK*
[b] *National Nuclear Laboratory, Chadwick House, Birchwood Park, Warrington, Cheshire, WA3 6AE, UK*
[c] *UKAEA, Culham Centre for Fusion Energy, Culham Science Centre, Abingdon, Oxfordshire, OX14 3DB*
**corresponding author: dk14424@bristol.ac.uk*

Abstract

Plasma-wall interactions in a commercial-scale fusion power station may exert high transient thermal loads on plasma-facing surfaces, repeatedly subjecting underlying structural materials to high temperatures for short durations. Specimens of the reduced activation ferritic-martensitic steel Eurofer-97 were continuously aged at constant temperature in the range of 550ºC to 950ºC for up to 168 hours in a furnace to investigate the microstructural effects of short-term high temperature exposure. A CO_2 laser was also used to repeatedly heat another specimen from 400ºC to 850°C a total of 1,480 times over a period of 41 hours to explore transient heating effects. Microstructural changes were studied via scanning electron and focused ion beam microscopy and include (i) the coarsening of Cr-rich secondary phase precipitates when continuously heated above 750°C (ii) an increase in average grain size above 800ºC and (iii) the evolution of a new lath martensite microstructure above 850ºC. Conversely, transient heating via laser was found to result in the decomposition of the as-received lath martensite structure into ferrite and Cr-rich carbide precipitates, accompanied by a significant increase in average grain size from 0.1-2 µm to 5-40 µm. Experimental analysis was supported by thermodynamic simulation of the equilibrium phase behaviour of Eurofer-97 in MatCalc and thermal finite element modelling of plasma-wall interaction heating on the water-cooled lithium-lead tritium breeding blanket concept in Comsol Multiphysics. Simulated thermal transients were found to significantly alter the microstructure of Eurofer-97 and the implications of this are discussed.

Keywords: Fusion, Martensite, Microstructure, Thermal Effects, Modelling

1. Introduction

High temperature plasmas are generated within magnetic confinement fusion devices - the fusion plasma within the International Thermonuclear Experimental Reactor (ITER) will reach temperatures of 150,000,000ºC, and the plasma-facing first wall will be exposed to temperatures of 350ºC - 550ºC during normal operation [1]. However, turbulent plasma phenomena such as edge localised modes (ELMs), blobs, or disruptions may result in plasma-wall interactions which temporarily raise the temperature of first wall materials beyond their design limits [2]–[4]. These events may occur thousands of times during the design life of a prototype fusion power station, and repeated strikes to the same surface may result in the accumulation of localised thermal damage and the degradation of underlying materials. The cumulative effects of plasma-wall interactions on the phase regimes, microstructure and material properties of novel fusion reactor materials must be thoroughly understood prior to their use. Plasma-facing components will also experience high fluxes of 14.1MeV neutrons [5]

that can damage materials through primary knock-on atom displacement cascades and transmutation [6]. Thus, the degradation mechanisms of first wall materials are likely to be complex.

Ferritic-martensitic 9Cr-1Mo steels are favoured candidate materials for structural applications in fusion reactors due to their excellent radiation swelling resistance and small 50ºC increase in ductile to brittle transition temperature (DBTT) under high neutron fluxes [7], [8]. Variants of this steel have been developed by the fusion community that replace elements such as Mo, Nb, and Ni with W, V, and Ta. This strategic substitution eliminates elements that are readily transmuted into long-lived radionuclides under neutron irradiation, as they would otherwise pose a challenge for decommissioning and radioactive waste disposal [9]. The resultant materials are known as reduced-activation ferritic-martensitic (RAFM) steels.

Eurofer-97 is the leading RAFM steel candidate for the European and UK fusion programmes. It is the structural material of choice for several ITER tritium breeding blanket test modules including the water-cooled lithium-lead (WCLL) and helium-cooled pebble-bed (HCPB) test breeder blankets [2]. Eurofer-97 is also extensively employed as a structural material in blanket designs for the EU Demonstration Power Station (EU DEMO), a future commercial-scale prototype fusion power station [3], [10]–[13]. Many breeder blanket designs for EU DEMO feature a first wall comprised of a Eurofer-97 structure armoured with a thin (2 mm) layer of tungsten to protect Eurofer-97 from plasma-wall interactions. The first wall in these designs is often actively cooled by pressurised water or gaseous helium passing through coolant channels within the Eurofer-97 structure [14].

In addition to tungsten armouring, the damaging transient thermal loads in EU DEMO may be mitigated by employing a number of plasma control measures, such as resonant magnetic perturbation (RMP) coils to control edge localised modes (ELMs), and massive gas injection (MGI) and/or shattered pellet injection (SPI) to mitigate disruptions. Estimated transient thermal loads from the literature are given in Table 1.

Table 1. Thermal loads on the EU DEMO first wall arising from plasma phenomena [14]–[19].

Mode/Excursion	*Peak Load* $MW\ m^{-2}$	*Frequency* *Hz*	*Duration* *ms*	*Impact Factor* $MJ\ (m^2\ s^{0.5})^{-1}$
Blobs	0.16 – 0.49	-	5 – 20	-
Unmitigated ELMs	0.6	1 – 0.8	0.6	4-8
Mitigated ELMs	0.1 – 0.2	26	1.2	-
Unmitigated Disruption	100 – 250	-	4	95-128
Mitigated Disruption	75	-	5-10	0.75

Thermal energy from these high magnitude, short duration thermal loads may propagate through the plasma-facing tungsten armour to the underlying Eurofer-97 structure, briefly heating it above the maximum temperature limit of 550°C [15]. Repeated exposure to these thermal loads over time may result in the significant evolution of Eurofer-97 microstructure, and lead to the eventual degradation of mechanical and corrosion-resistant properties. This paper explores the effects of short-term high temperature exposure on the microstructure of Eurofer-97 and the effects of both continuous and transient heating.

Prior work on the thermal aging of Eurofer-97 has been previously undertaken by others, but with little consideration of transient thermal loads and at considerably lower temperatures than those explored here [20], [21]. Additionally, high temperature studies on conventional 9-12Cr ferritic-martensitic steels are not directly comparable due to the novel composition and unique phase behaviour of Eurofer-97. Fernandez et al. aged Eurofer-97 at 400°C, 500°C and 600°C for 1000, 5000 and 10,000 hours and observed Cr enrichment at grain boundaries [20]. This was attributed to the presence of $M_{23}C_6$ chromium precipitates located along grain and sub-grain boundaries, but they did not discount the possibility of Cr diffusion to grain boundaries [20]. The mechanical properties of Eurofer-97 were found to be stable at temperatures up to 600°C, with a 23ºC increase in the DBTT perhaps linked to the observation of occasional equiaxed grains replacing martensitic laths. This was attributed to Cr precipitate coarsening's effect on the pinning and mobility of lath interfaces reported in 9Cr-1Mo steels [22]. Areas of recrystallisation occurred in F82H steel but overall a similar lack of significant microstructural change was seen in 7-11CrW reduced activation martensitic steels exposed to 250-550°C for up to 13,500 hours [23].

The temperatures explored in this study may occur under off-normal conditions and for relatively short durations, but small successive changes to the microstructure of Eurofer-97 may accumulate over time and gradually degrade essential material properties. Structural integrity is an important safety concern for water-cooled tritium breeding blanket concepts, due to the explosion risk posed by hydrogen-producing lithium-water interactions, and the radiological hazard to workers posed by retained tritium in plasma facing materials [15]. Understanding how Eurofer-97 behaves under reactor-like conditions will be vital to developing a robust safety case for EU DEMO, and will have important implications for the reliability, availability and economic basis of future fusion power stations.

2. Computational Modelling

2.1 Thermal Transients arising from Plasma-Wall Interactions

A simulation of mitigated disruption heating on the first wall of the 2019 single module segment (SMS) WCLL breeder blanket for EU DEMO (Fig. 1(a)) was undertaken to determine target parameters for the thermal exposure experiments in Section 3. The COMSOL Multiphysics 2019 software was used to perform thermal finite element analysis on a defeatured 2D representation of the WCLL first wall. A time-dependent study with step increments of 0.1 ms was employed with thermal properties from the literature [24]. Thermal stresses were not calculated.

The model of the WCLL first wall was discretised into a mesh of 2,200 2D triangular planar linear heat transfer elements. Element edge length varied from 7.00–0.01 mm with smaller elements employed at the tungsten-Eurofer-97 interface to improve local precision. Boundary conditions and interaction properties were configured based on the following assumptions:

- Toroidal symmetry (plane heat transfer).
- Thermal resistance across the tungsten-Eurofer-97 interface is negligible.
- The thermal mass of the PbLi tritium breeding material is such that it is unaffected by disruption heating and remains at a constant initial temperature of 400°C [24].

- Water velocity in the first wall cooling channels is 2.0 m s^{-1}. This yields a convective film coefficient at the cooling water-Eurofer-97 interface of 21,350 W m^{-2} K^{-1} using the Dittus and Boelter [25].
- The water in the first wall cooling channels at 155 bar does not exceed its saturation temperature of 345°C and remains single-phase.

To verify material properties, geometry and boundary conditions, normal operation steady state thermal loads were applied to the model from recent literature on WCLL development [26], [27]. The simulation was checked for convergence using the maximum temperature of Eurofer-97 and validated against literature values. The model was found to converge on a solution for maximum Eurofer-97 temperature that agreed with the literature to within ±5°C [24]. To simulate mitigated disruption heating the steady state was perturbed by a heat flux of 75 MW m^{-2} applied to the plasma-facing tungsten surface for a duration of 10 ms [15]. The resulting change in temperature of the Eurofer-97 components was studied.

The simulation revealed that despite the tungsten armour, the temperature of Eurofer-97 regions of the WCLL first wall increases from the normal average operating temperature of 400°C to a maximum of 853°C during a mitigated disruption (Fig. 1(c)). This temperature rise occurs in under a second due to the high thermal conductivity of the thin 2 mm plasma-facing tungsten layer (150 W K^{-1} m^{-1}) [28]. However, it is short lived (Fig. 1(b)) and thermal energy is quickly removed from the affected area by the first wall water cooling channels and the PbLi tritium breeder material.

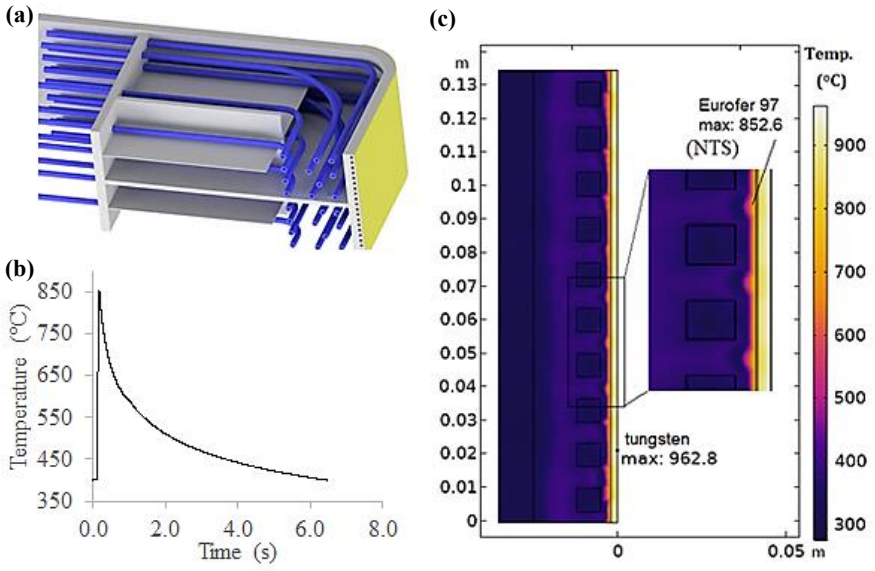

FIG. 1. (a) Cut-away 3D model of the WCLL breeding blanket with plasma-facing tungsten surface in yellow (b) Plot of maximum WCLL first wall Eurofer-97 temperature versus time during (and after) a mitigated disruption occurring at 0.1s. c) Temperature distribution in the WCLL first wall 0.1 ms after a mitigated disruption.

Commented [HDA1]: I would add top and right axis like on the other plots of the paper to maintain consistency.
Also I would change the colour ot the line to something more eye catching like blue. And maybe increase the thickness a little bit.

The maximum Eurofer-97 temperature is observed at the tungsten-Eurofer interface, where residual stresses from the tungsten joining process may be present and tritium adsorption from the plasma may occur. It is also proximate to the square water-cooling channels of the first wall, where the corrosion-resistance of Eurofer-97 will be of principal concern.

2.2 Eurofer-97 Phase Evolution

To gain insights into the phase evolution of Eurofer-97, MatCalc thermodynamic modelling software was used to calculate the equilibrium phase fraction diagram of Eurofer-97 with composition 8.89Cr – 1.11W - 0.44Mn - 0.19V – 0.14Ta - 0.12C (wt.%) from Table 2. MatCalc is based on the CALPHAD (Computer Coupling of Phase Diagrams and Thermochemistry) method for thermodynamic calculations.

Table 2. Composition of Eurofer-97 from literature [13].

Element	Weight %
Cr	8.82 – 8.96
W	1.07 – 1.15
Ta	0.13 – 0.15
V	0.18 – 0.20
Mn	0.38 – 0.49
C	0.11 – 0.12
Fe	Bal

The literature composition of Eurofer-97 was used to obtain the equilibrium phase fraction diagram from MatCalc in Fig. 2. A significant point can be seen at ~800ºC where the phase fraction of ferrite drops to zero and new austenite forms. At this point the fraction of $M_{23}C_6$ precipitates decreases to zero as the precipitates are taken into solution, but TaC precipitates are still present. The formation of new martensite in prior austenite grains is expected to occur as specimens are cooled from austenite temperatures to below the martensite onset temperature of 360ºC [29]. Martensite is a metastable phase and therefore not present in the equilibrium phase fraction diagram.

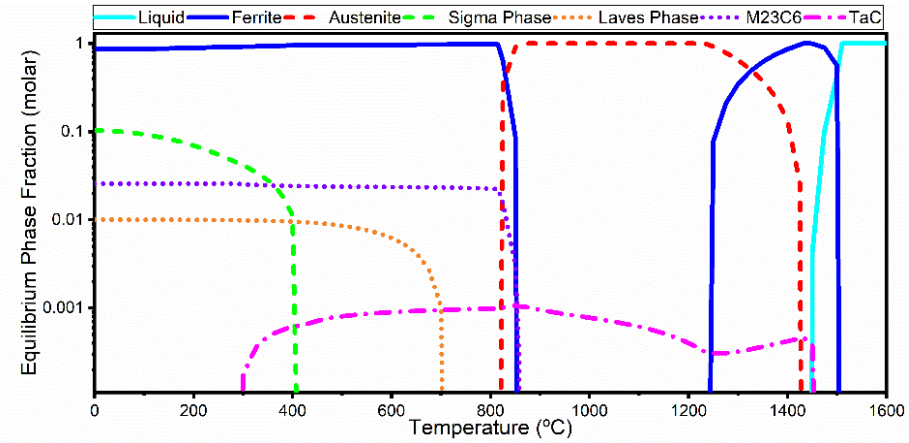

FIG. 2. MatCalc equilibrium phase fraction diagram for Eurofer-97.

3. Experimental Procedure

3.1. Heat Treatment

A block of untreated Eurofer-97 cast 2 with composition 9.08Cr-1.07W-0.23V-0.12Ta-0.56Mn-0.10C (in wt.%) [29] was provided by United Kingdom Atomic Energy Authority (UKAEA), Oxfordshire, UK. Two sets of samples were prepared from this material using a Struers Accutom 50 diamond disc cut-off saw. Throughout sectioning, the workpiece was water cooled and the saw feed rate limited to 0.05 mm min^{-1} to minimise cutting damage. The first set of samples were cut to 6 x 4 x 2 mm^3 for use with a continuous heating experiment. These samples were sealed under vacuum in quartz vials and degassed at 680ºC. Samples were subjected to temperatures of 550ºC, 650ºC, 700ºC, 750ºC, 800ºC, 850ºC, and 950ºC for 168 hours. 850ºC and 950ºC samples were then revisited to explore shorter 4 hour and 24 hour exposures. After ageing the sealed vials were removed and quenched in water.

Commented [DH2]: Suggested change. This will be confirmed by pinboard – but think this is preferable to CCFE

The second set of Eurofer-97 samples were cut to 8 x 8 x 0.5 mm^3 for use with a transient heating experiment. This employed a laser heating apparatus (Fig 3.) that directly applies beam to the sample, enabling rapid and controllable heating. The laser used (Synrad Inc, Firestar V40 series) was a continuous wave CO_2 laser (λ = 10.6 µm) with linear polarisation and an output power of 40 W. System optical losses are estimated to be 25% thus the maximum power applied to the laser-incident sample face was approximately 30 W. More details about this system can be found elsewhere [31].

Preliminary testing found the laser absorption of the as-prepared Eurofer-97 sample insufficient to rapidly reach the representative maximum temperature predicted by the thermal simulation (Section 2). To improve the laser-material interaction a plasmonic grating coupler was fabricated on each laser-incident face. This was comprised of a laser-engraved linear grating on the Eurofer-97 with a period of 10.5 µm and a filling factor of 50%, coated with 50 nm of tungsten via DC magnetron sputtering [32]. The tungsten coating being necessary as steel alloys don't have plasmonic properties, contrary to tungsten. Reverse (non-laser incident) faces were polished to reduce their emissivity and lower radiative heating losses, and the sample holder was made of quartz to minimise conductive heat losses.

Samples of Eurofer-97 with the plasmonic grating coupler were rapidly heated by the laser apparatus from a base temperature of 400°C to 850°C by operating the laser at full power for 12 s, then passively cooled to 400°C via radiation to the vacuum chamber internals and conduction to the quartz sample holder. This was repeated 1,480 times over a total of 41 hours.

Sample oxidation during high-temperature exposure was minimised by conducting the experiment under vacuum with a chamber base pressure of 7.5×10^{-5} mTorr. The temperature of the laser-incident sample face was continuously monitored throughout the experiment by a non-contact dual-detector (λ = 1.0, 1.5 µm) infrared spot pyrometer, operated in single colour mode. This instrument has a resolution of 0.1°C and a maximum uncertainty of 2°C. The emissivity of tungsten used (ε = 0.35) was based on literature values [33].

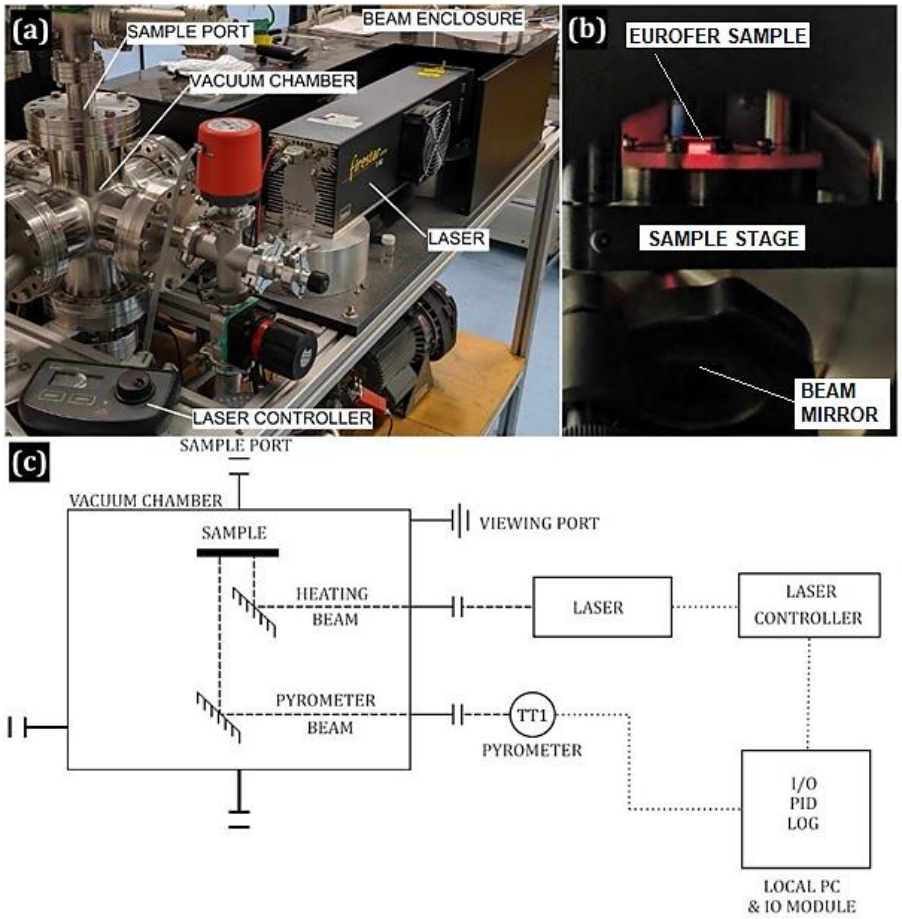

FIG. 3. a) An annotated photograph of the laser apparatus used for transient thermal exposure. b) A sample of Eurofer-97 on the sample stage, glowing red during laser exposure c) Diagram of the laser heating apparatus.

240

3.2. Specimen Preparation for Microstructural Characterisation

Heat treated specimens were prepared for microstructural analysis by mounting in conductive thermosetting resin and sequential polishing using progressively finer SiC papers to a 5 µm finish, and then subsequently to a 1/4 µm diamond polish in accordance with [34]. A 12 hour 50 nm colloidal silica vibrational polish was used to obtain the final mirror finish. Between each grinding and polishing stage, samples were throughly cleaned with detergent to avoid cross-contamination between grits/pastes. At the end of polishing, samples were ultasonically cleaned and degreased using acetone, ethanol, isopropanol, and distilled water.

250

3.3. Characterisation Techniques

A Zeiss SigmaHD Variable Pressure Field Emission Gun Scanning Electron Microscope (FEGSEM) equipped with secondary electron (SE), angle selective backscatter (AsB), energy dispersive X-ray (EDX), and electron backscatter detector (EBSD) was used for the characterisation of microstructure. Beam acceleration voltages of 10-20kV were employed for imaging. EBSD data was collected with the specimen tilted at 70° to the electron beam, using a voltage fo 30kV and a 120µm apperature. EBSD data were collected using a DigiView 3 high-speed camera, run using using orientation image mapping (OIM) software (Ametek, Utah, USA).

Focused Ion Beam (FIB) milling was performed using a FEI FIB 201. A 12 nA/30 kV ion beam was used to remove surface oxide from the specimens, which is determined as the point where ion-channelling grain contrast becomes visible. A 150 pA/30 kV beam was used to image the grain structure, prior to the introduction of XeF_2 gas into the chamber. With the beam blanked, gas flow was initiated and allowed to reach a partial pressure of $1.5x10^{-5}$ mbar before the flow was stopped. After a few seconds of rapid beam scanning at 150 pA/30 kV to allow for excess-gas to be sputtered away, imaging was resumed. As per previous work [35] the XeF_2 adhered to the oxide-free metal surface and not the carbide precipitates. Whilst a full description of the process is beyond the scope of this paper, the XeF_2 gas increases the secondary electron yield of the metal surface and improves contrast to highlight the carbides. Counting statistics were obtained using a series of simple image processing tools, including a custom LabView script for area % counting. This used thresholds of 50 pixels and 125 pixels to define between coarse, intermediate/agglomerate, and fine precipitates. These correspond to feature diameters of ~470 nm and ~740 nm respectively, assuming a spherical precipitate. Particle sizes were chosen arbitrarily in order to distinguish between single large precipitates and agglomerations of smaller precipitates forming the 'intermediate' group.

4. Results

4.1 Microstructure of As-received Eurofer-97

Fig. 4. shows that as-received (AR) Eurofer-97 has a normalised tempered martensitic microstructure with martensite laths of length 0.1 - 2 µm occurring in prior austenite grains with diameters of 5-12 µm. The XeF_2 enhanced FIB imaging (Fig. 4.b) reveals the homogeneous distribution of ~400 nm diameter carbide precipitates preferentially at prior austenite grain boundaries [35]. An EBSD scan (Fig 4.c) shows the as-received microstructure to be isotropic with a high degree of homogeneity.

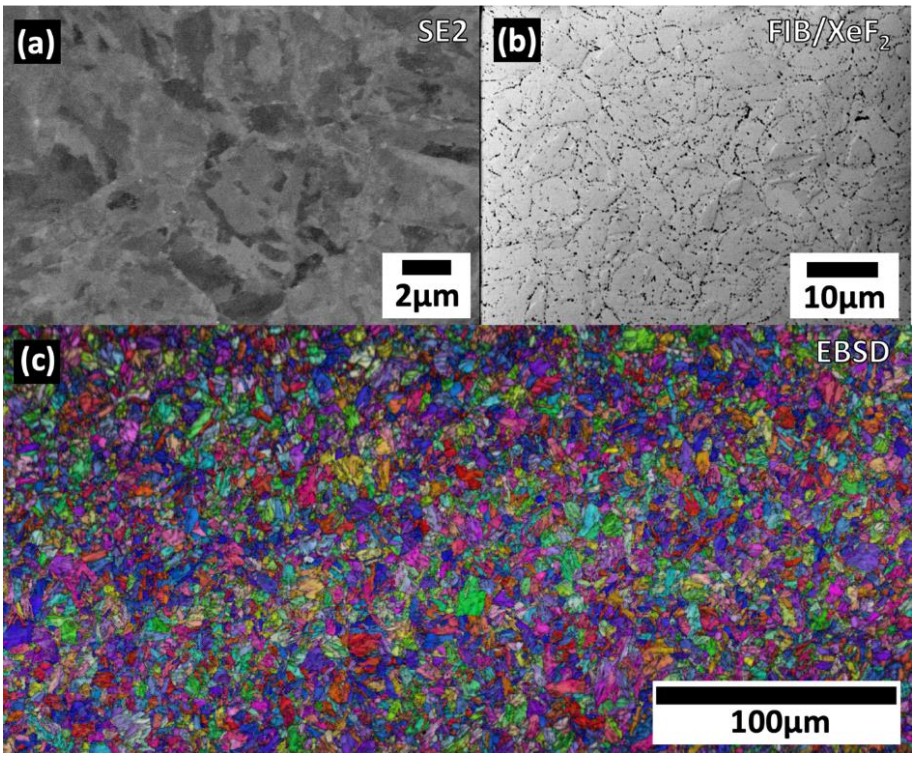

FIG. 4. As-received Eurofer-97 imaged with: (a) SEM secondary electron detection; (b) XeF_2 enhanced FIB with carbides in black; (c) EBSD grain orientation map.

Commented [DH3]: Fig 4 had no full stop at the end

4.2 Furnace-aged Eurofer-97

No significant microstructural change was observed for Eurofer-97 thermally aged at 550ºC and 650ºC for 168 hrs compared with the as-received condition. However, using XeF_2 enhanced FIB imaging in Fig. 5. reveals that there is secondary phase coarsening at higher temperatures up to 800ºC. Fig. 5. shows samples aged for 168 hours at 700 - 800ºC with XeF_2 enhanced FIB imaging. The right hand column highlights grain structure of aged samples as XeF_2 is etched away whilst the left hand column highlights secondary phase precipitates due to XeF_2 adherence to the bulk [35]. EDX of secondary phase precipitates shows they are Cr-rich with compositions ranging from 20 wt.% at 750ºC up to 30 wt.% for the largest precipitates at 800ºC compared to ~8.89 wt.% in the overall composition from Table 2.

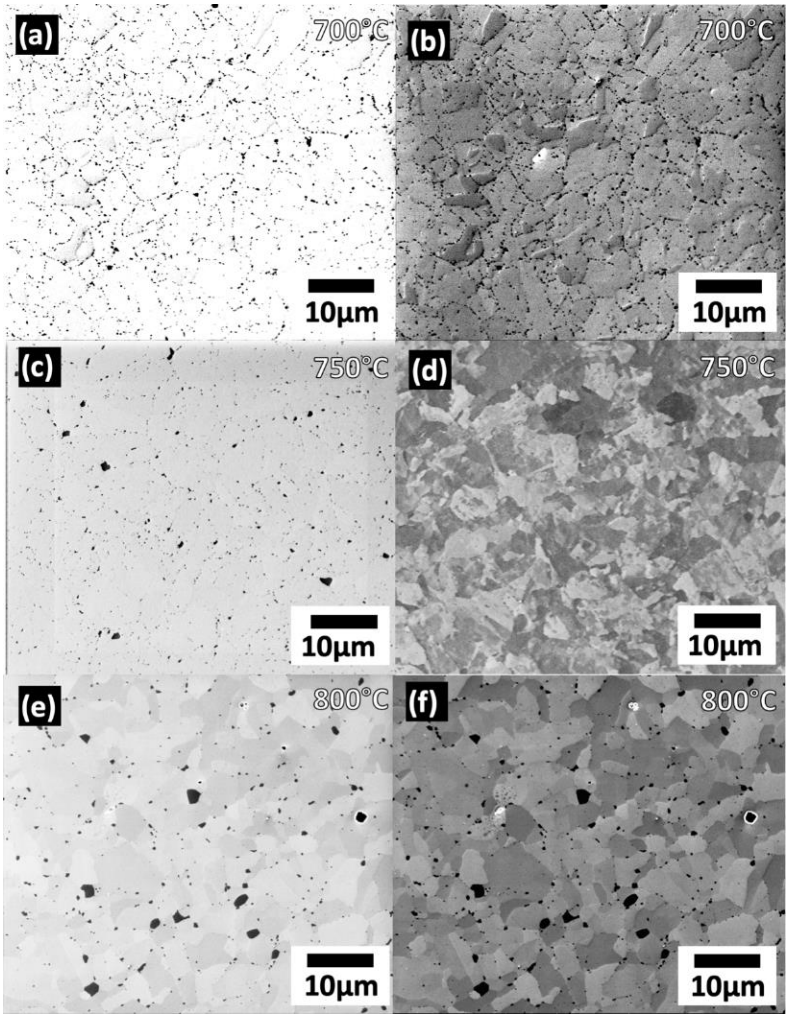

FIG. 5. XeF_2 enhanced FIB images of Eurofer-97 thermally aged for 168 hours at (a,b) 700ºC, (c,d) 750ºC, and (e,f) 800ºC. Left column highlights precipitates in black from XeF_2 enhanced FIB imaging. Right column highlights grain structure as XeF_2 layer is etched away.

Fig. 6. shows the counting statistics obtained from the analysis of the precipitate sizes in the XeF_2 enhanced FIB data in Fig. 4.b and Fig. 5. Precipitates are grouped into small (< ~470 nm diameter), intermediate, and large (> ~740 nm diameter). Fig. 6. shows the fraction of total precipitates present in each sample fall into which size category. The total percentage area of the surface covered by secondary phase precipitates is also shown in the top right corner.

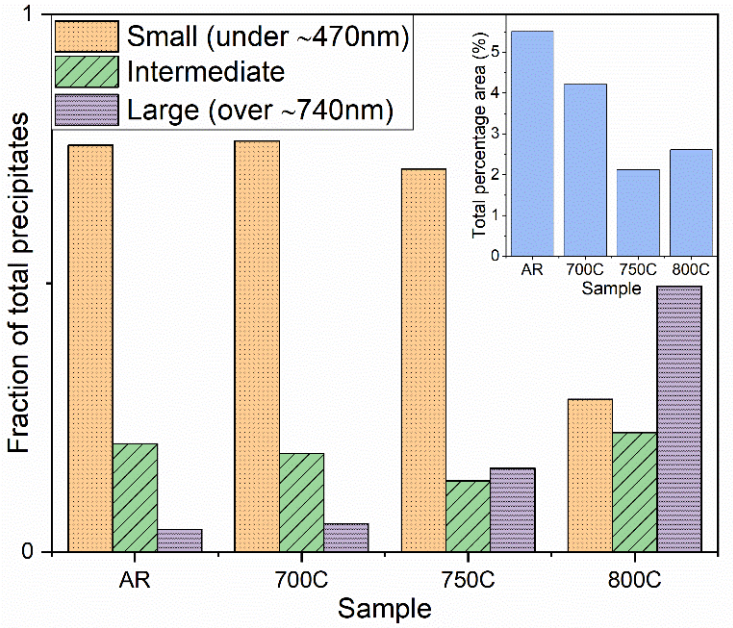

FIG. 6. Counting statistics taken from Fig. 4.b and Fig. 5.a, c, e XeF_2 enhanced FIB images highlighting secondary phase precipitates. Precipitates distinguished by small (< ~470 nm), intermediate, and large (> ~740 nm). Figure shows fraction of total particles in each category and the total percentage area taken up by secondary phase precipitates.

It is also observed in Fig. 7 that Eurofer-97 aged for 168 hours at 800ºC results regions with significantly larger grains (~100 µm) than those of the as-received Eurofer-97 (< 10 µm Fig. 4). Fig. 7.d shows the same FIB imaged area as that in Fig. 7.c but with XeF_2 introduced to highlight the coarsened precipitates. Fig. 7.e,f show the concentration of Cr and W in these precipitates via EDX. Point spectra taken from precipitates in Fig. 7.e,f gave a Cr concentration of (19 ± 2) wt.% and (3.1 ± 0.5) wt.% for W compared to 8.89 wt.% and 1.11 wt.% expected from Table 2.

Fig. 8.c shows that after 168 hours at 850ºC the microstructure changes significantly to a new martensitic lath structure with few misaligned ferrite grains remaining. Fig. 8.a,b show the progression of this change at shorter durations (4 hours, 24 hours). We also note the presence of a Cr secondary phase after 168 hours similar in size to those after 168 hours at 800ºC (Fig. 8.d).

Commented [DH4]: Missing a space

After 168 hours at the highest investigated temperature, 950ºC, we see a fully martensitic structure in prior-austenite grains (Fig. 9). This structure is also seen after shorter durations (24hours) in Fig. 9.a,b. The Cr-rich precipitates have dissolved completely with only small ~100 nm diameter Ta-rich MX precipitates found via EDX with 6 – 12 wt.% vs bulk (0.15 ± 0.34) wt.%.

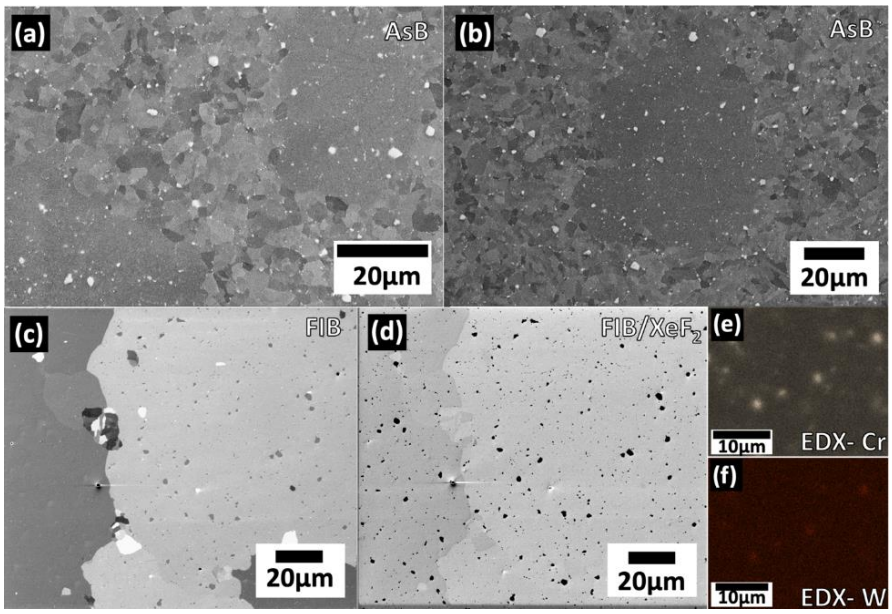

FIG. 7. Eurofer-97 samples aged for 168 hours at 800ºC. (a) and (b) SEM images with backscatter detector. Cr-rich precipitates in white. (c) FIB image of large grain region. (d) XeF_2 enhanced FIB of the same region, highlighting Cr-rich precipitates. (e,f) EDX maps showing concentration of Cr and W respectively in precipitates.

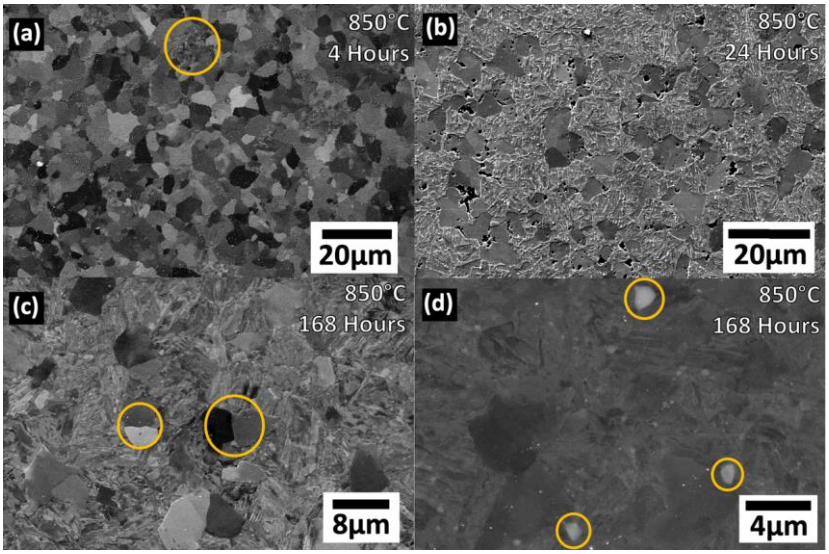

FIG. 8. Eurofer-97 heat treated at 850ºC for (a) 4 hours, pocket of martensite circled. (b) 24 hours, increased formation of new martensite. (c) 168 hours, mostly martensite with misaligned ferrite grain pairs circled. (d) Backscatter image after 168 hours. Cr-rich secondary phases circled, largest with diameter ~1700nm.

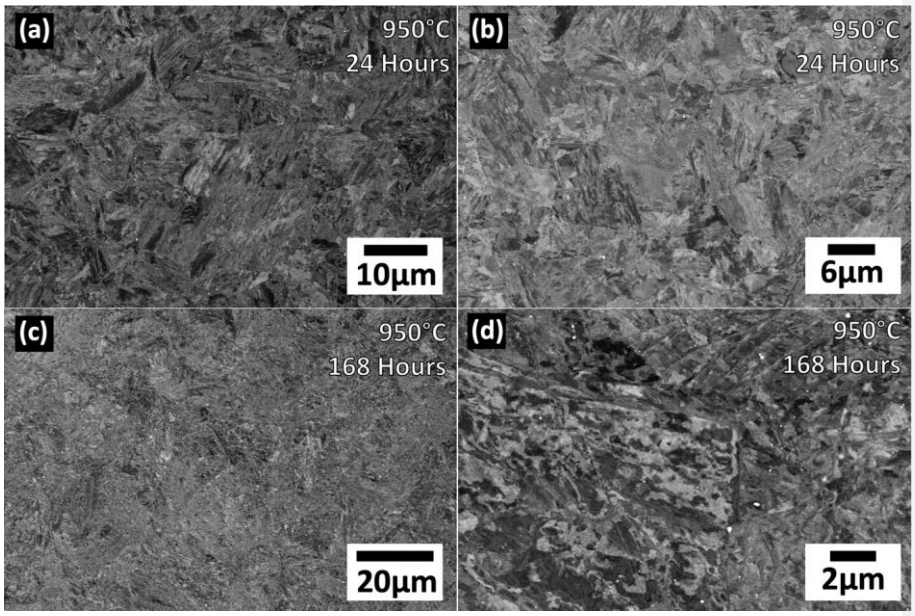

FIG. 9. Eurofer-97 SEM secondary electron images of sample heat treated at 950ºC for (a,b) 24 hours and (c,d) 168 hours showing new martensitic lath structure in prior austenite grains.

4.3 Laser-exposed Eurofer-97

The CO_2 laser was used to heat a representative 8 x 8 x 0.5 mm sample of Eurofer-97 from 400°C to ~850°C in ~15 seconds. This was repeated a total of 1,480 times over 41 hours, with the sample allowed to cool down to 400°C via radiation to sample chamber walls before each repeat. The mean peak sample temperature was 846°C (SD = 14.7°C). The repetition rate was limited by cooling time which resulted in a mean transient event duration (including cooling time) of 104 seconds. Fig. 10 shows a subset of the temperature readings obtained during 10 simulated mitigated disruptions.

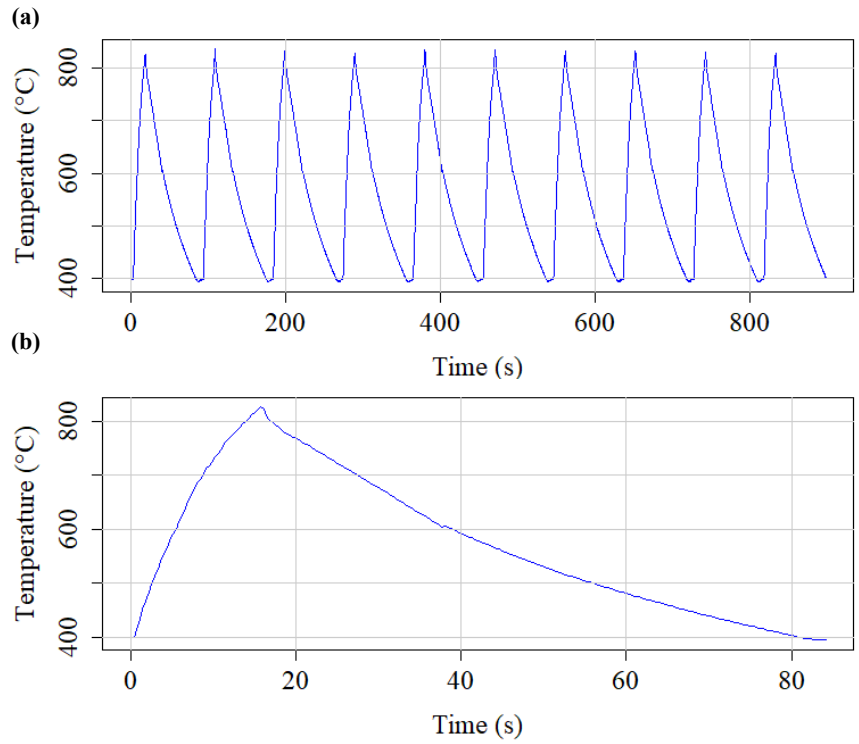

Commented [DK5]: Inset fig of one of the peaks zoomed in

FIG. 10. Pyrometer measurements of Eurofer-97 sample temperature during a) 10 of the 1,480 transient heating events, b) a single heating event.

Characterisation (Fig. 11) of Eurofer-97 exposed to 1,480 transient heating events revealed a significant grain size increase versus the as-received Eurofer-97. Grain size was measured by the ImageJ software and the average was found to have increased from 0.1 - 2 µm to 5 - 40 µm. Additionally, the characteristic martensite laths observed in Fig. 4 were notably absent, and the microstructure was found to have transformed to ferrite plus carbide precipitates (Fig. 11). New coarsened precipitates were found to be abundantly distributed throughout the laser exposed Eurofer-97 and were located at both grain boundaries (intergranular) and inside ferrite grains (intragranular). The precipitates were found to be Cr-rich (Fig. 11.e) with typical composition shown in Table 3.

Table 3. Composition of a typical Cr-rich precipitate post laser exposure (from EDX).

Element	Weight %
C	1.54
N	2.82
O	1.2
V	0.65
Cr	17.07

Fe	74.4
Ta	0.4
W	1.92

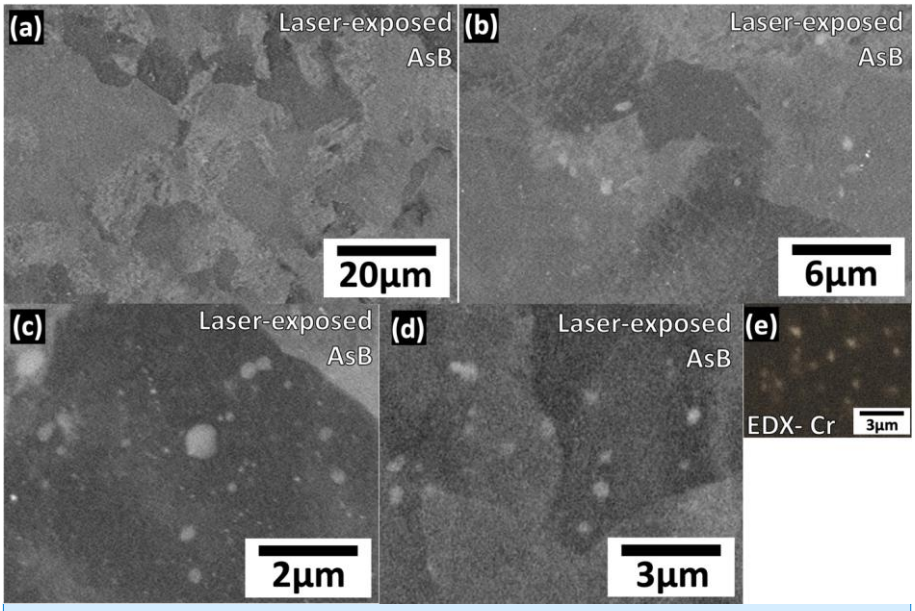

FIG. 11. AsB micrographs of laser-exposed Eurofer-97 at: (a) 1kX, (b) 5kX, (c) 10kX, and (d) 15kX. (e) EDX map of the same region as (d) showing Cr concentration.

Commented [DH6]: No full stop at end of fig 11 caption

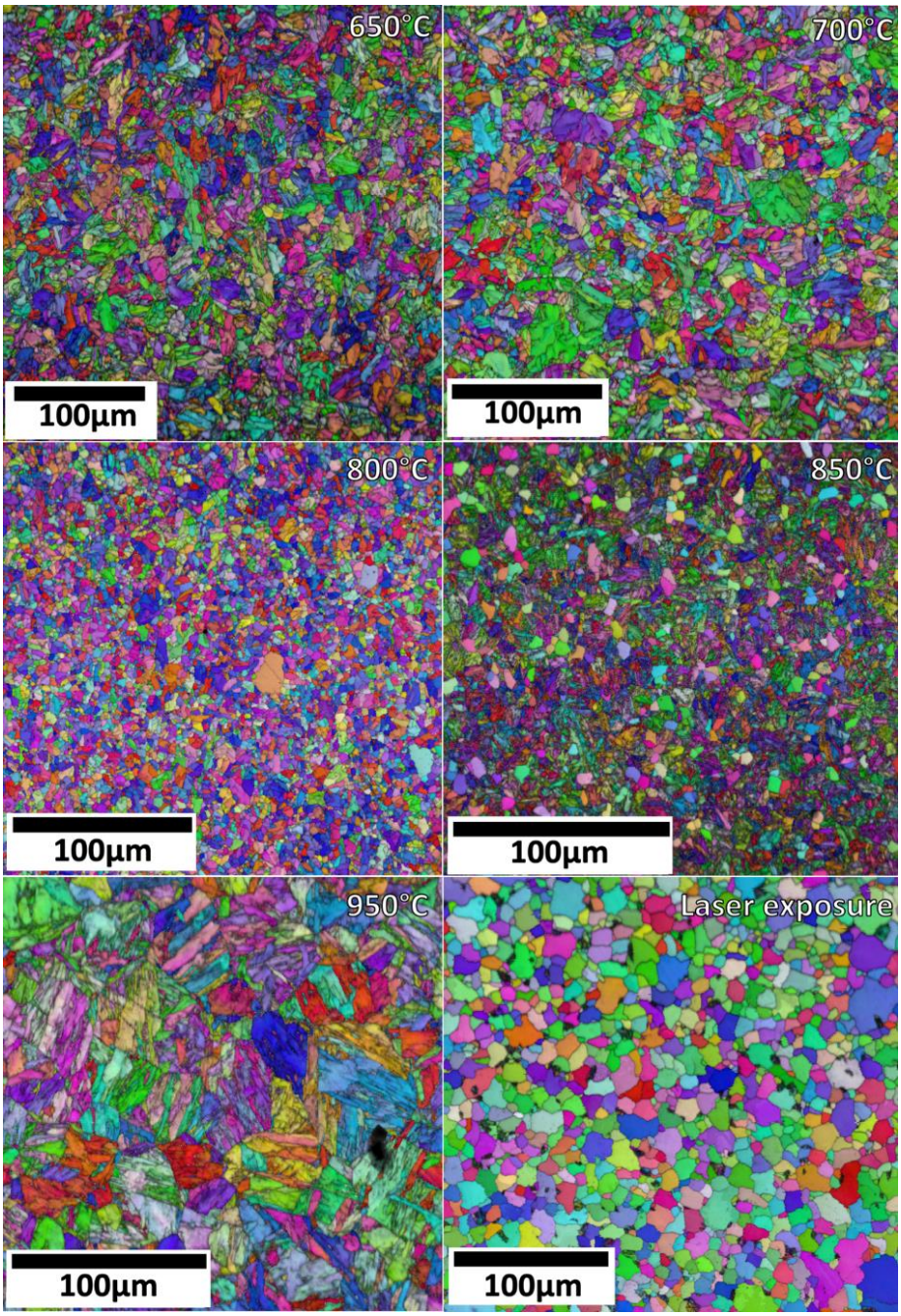

FIG. 12. EBSD grain orientation maps for samples aged in furnace experiments for 168 hours as well as for the laser-exposed sample.

Fig. 12. shows EBSD grain orientation maps for samples aged in the furnace for 168 hours in comparison to the laser-exposed sample. At 650ºC and 700ºC the tempered martensitic lath structure was seen to be similar to that of the as-received sample (Fig. 4.c), although with approximately 2x larger mean grain diameter. At 800ºC larger (~16 µm) grains are present amongst a sea of smaller (mean of ~5 µm) equiaxed grains as we observe less of the as-received lath structure. At 850ºC there is a clear transformation to new martensitic laths in prior austenite grains, but some ferrite remains. There is then a fully martensitic structure observable at 950ºC. The laser-exposed sample differs from the furnace samples where it is seen to have significantly larger (mean of ~19 µm) equiaxial ferrite grains.

Fig. 13 shows how grain diameter has changed with the heat treatments. Grain diameters of the samples furnace aged for 168 hours at 800ºC and 850ºC are not dissimilar to the as-received grain size with most below 10 µm, despite the original martensitic lath structure subsiding for equiaxed ferrite grains at 800ºC and the presence of new martensite at 850ºC in Fig. 12. The sample aged at 950ºC for 168 hours and the laser exposed sample exhibit the largest increase in grain diameter from the as-received specimen. For the 950ºC furnace sample this contribution appears to be from the new martensitic laths forming in large (mean of ~17 µm) prior-austenite grains. The laths themselves are longer than other samples but narrow compared to the large equiaxed ferrite grains seen in the laser exposed Eurofer-97. The average grain size in the laser exposed sample is ~19 µm compared to ~4 µm for the as-received sample, nearly a 5x increase.

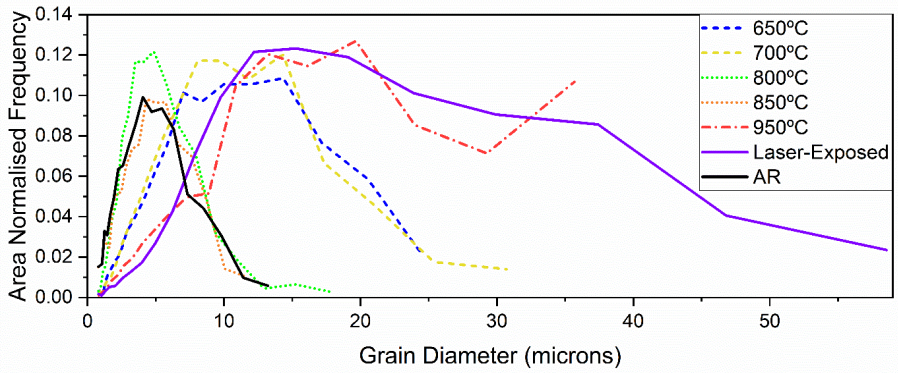

FIG. 13. Area normalised frequency vs. grain diameter obtained from EBSD data for furnace samples aged for 168 hours and the laser-exposed sample (as in Fig. 12) compared to the as-received sample (Fig.4.c).

5. Discussion

The results show the effects of continuous and transient short-term exposure of Eurofer-97 to simulated first wall temperatures predicted during a mitigated disruption in DEMO. Major observed microstructural changes include (i) the coarsening of secondary phase precipitates up to 800ºC, (ii) the decomposition of the tempered martensite structure, and (iii) significantly increased average grain sizes.

EDX analysis of secondary phase precipitates in both furnace-aged (Fig. 7.e,f) and laser exposed samples (Fig. 11.e) revealed them to be Cr-rich. Eurofer-97's equilibrium phase diagram (Fig. 2) suggests that these precipitates are either $M_{23}C_6$ or TaC carbides. Fig. 5.a,c, e reveals that precipitates grow larger as the heat treatment temperature increases, leading to a sparse distribution of larger carbides (up to ~2 µm diameter) after 168 hours at 800°C. Particle counting analysis of furnace aged samples (Fig. 6) revealed a decrease in the total percentage area of secondary phase precipitates from the as-received sample to that aged at 750ºC for 168 hours from 5.51% area to 2.12% area. The percentage area increased slightly for the 800ºC aged sample to 2.61% area where the majority of particles are now 'large' (> ~740 nm). Below 800ºC the number of 'large' particles increases with the temperature of heat treatments, but the main contribution to the total percentage area was from 'small' (< ~470 nm) particles. Overall, analysis confirms the observation of coarsening of Cr rich precipitates and a decrease in the proportion of smaller carbides. As precipitates coarsen with temperature the overall area covered by secondary phases decreases. Conversely, precipitates in F82H steel under irradiation have been found to decrease in size potentially resulting in two competing processes at play for Euforer-97 within the fusion reactor [36], [37]. After 168 hours at 950ºC, coarse Cr rich precipitates are no longer present and only small (~100 nm) Ta-rich precipitates remain. Looking at the equilibrium phases expected this temperature (Fig. 2), it implies that these remaining Ta-rich precipitates are TaC precipitates and that the previous coarse Cr-rich precipitates were $M_{23}C_6$ that are no longer present at 950ºC.

For samples aged for 168 hours at different temperatures, microstructural changes were observed in line with MatCalc thermodynamic modelling. Fig. 2 shows that there should be no new phases observed below ~800ºC and that ferrite is the bulk equilibrium phase. This is confirmed by Fig. 12 where the tempered ferritic-martensitic structure remains after 168 hours 650ºC and 750ºC and we see equiaxial ferrite grains at 800ºC as the as-received microstructure begins to decompose. Above this temperature austenite should begin to form as the new equilibrium phase (Fig. 2) which, upon quenching, instantaneously transforms into a metastable martensitic lath structure. This new martensite formation is seen in samples aged for 168 hours at 850ºC and 950ºC (Figs. 8, 9, 12) and is far more brittle than the as-received tempered ferritic-martensitic structure due to the increased number of interfaces inhibiting dislocation movement. Fig. 13 indicates how these phase changes affect the grain size. After 168 hours at 650ºC and 750ºC the grain sizes are seen to have increased by approximately 2x as energy enters the system but no new phases precipitate leading to existing grains coarsening. Conversely, after 168 hours at 800ºC and 850ºC the average grain size remains similar to that of the as-received sample (Fig. 13) but we are at the point where an equilibrium phase change to austenite is expected (Fig. 2). Here a new phase precipitates but the overall grain diameter of the new phase has not changed from as-received. After 168 hours at 950ºC we have transitioned fully to new martensite in prior austenite grains that are, on average, over ~3x larger in diameter than the as-received tempered ferritic-martensitic grains as there is greater energy in the system.

Commented [DH7]: Should be no space – none earlier in paper

Commented [DH8]: No space needed again for consistency

For high temperature furnace exposures, changes were also observed after shorter durations. Packets of new martensite were seen after just 4 hours at 850ºC with the transition to new martensite in prior austenite grains seen progressing after 24 hours (Fig. 8.a, b). Thermodynamic modelling suggests austenite and TaC should be the equilibrium phases at this temperature (Fig. 2) which implies these short durations are not enough to achieve total equilibrium. This is seen as misoriented ferrite grains and suspected coarse $M_{23}C_6$ precipitates still remain after 168 hours (Fig. 8.c, d) where they should no longer be present (Fig. 2). At 950ºC the microstructure is fully martensite after only 24 hours (Fig. 9.a, b). This shows that even short exposures to the higher temperatures can results in significant microstructural change.

Commented [DH9]: Consistency

Greater changes in grain structure are seen in Fig. 7 (furnace aged at 800ºC for 168 h) and Fig.11 (laser-exposed to 850°C, 1,480 times). Though grain size was seen, on average, to not differ greatly from as-received for 168 hours at 800ºC (mean of ~4 µm, Fig. 13), there are regions of this sample where grains up to ~100 µm in diameter are seen (Fig. 7). Likewise, in the laser exposed samples grains are seen to span a much larger range of sizes from 5 – 40 µm (Fig. 13). These effects could be due to recrystallised sub-grains merging, as 800ºC is close to the ferrite-austenite transition temperature (Fig. 2). Both the furnace and laser-exposed samples were exposed to 800/850°C for relatively short durations, thus recrystallisation was likely interrupted before thermodynamic equilibrium could be reached. Fig. 7.c, d reveals that the distribution of the coarsened precipitates does not follow the boundaries of the new larger grains but are intragranular, providing an indication of the pre-recrystallisation grain structure. In practice, the laser-exposed sample spends the majority of the time at temperatures below 800/850ºC (Fig. 10) which is where grain sizes were seen to increase ~2x from as-received shown previously for furnaced aged samples (Fig. 13). Therefore, more time spent in this lower temperature regime could explain why we observe 5 – 40 µm equiaxial ferrite grains coarsening, leading to decomposition of desired ferritic-martensitic microstructure, and no new phases forming.

Commented [DH10]: consistency

In the laser experiment, the sample of Eurofer-97 was allowed to naturally cool to its normal in-service operating temperature of 400°C between laser shots, instead of being quenched to room temperature at the end of the experiment. This extra cooling will have limited the extent to which recrystallization can occur and accelerated both ferrite grain growth and the decomposition of the martensite phase. This is an important finding as it may be more closely analogous to in-reactor conditions. There is scope for future work to further explore this - the laser apparatus could be modified with a cooling system to enable cooling rates of Eurofer-97 samples to more closely match those estimated by the simulation work.

Understanding the role of plasma-wall interactions in the long-term degradation of first wall structural materials is an essential step in developing a robust safety case for EU DEMO. Coarsening of Cr-rich secondary phases, formation of new martensite in prior austenite grains, and increases in grain size are all changes that could affect mechanical properties of Eurofer-97. Larger grain sizes and carbide coarsening would increase dislocation movement and coarsening of Cr-rich precipitates could also affect corrosion behaviour pertinent to WCLL breeder blanket design. Secondary phase carbides may also contribute to the pinning of martensitic laths, therefore coarsening may accelerate the decomposition of the as-received tempered martensitic microstructure [22], [23]. Also high temperature creep behaviour may be affected, as grain boundary carbides have been found to promote the nucleation and growth of intergranular creep cavities [38].

Future work could explore transient heating effects on oxide dispersion strengthened (ODS) Eurofer-97, a variant that employs a homogenous dispersion of nano oxides to improve high temperature creep behaviour, as the implications of results presented here on ODS Eurofer-97 are not yet known. Presently, nearly all leading candidates for breeder blankets of EU DEMO employ conventional Eurofer-97 steel [3], [10]–[13].

6. Conclusions and Scope for Further Work

6.1 Conclusions

Breeder-blanket structural materials in nuclear fusion reactors may be exposed to higher than normal operating temperatures up to 850ºC as a result of plasma-first wall contact events. Eurofer-97 components of the DEMO first wall are predicted to briefly reach such temperatures during mitigated plasma disruptions, which may occur thousands of times during a DEMO plasma campaign. Specimens of Eurofer-97 were thermally aged in a furnace for 168 hours up to 950ºC as well as heated via a pulsed CO_2 laser in order to simulate the effect of thermal transients.

The microstructure of Eurofer-97 has been found to be significantly altered by 168 hour exposures to temperatures between 650°C and 950°C. After 168 hours at 650ºC and 750ºC the average grain diameter was seen to have approximately doubled. From 700ºC to 800ºC coarsening of Cr-rich secondary phase precipitates was observed. Above 850ºC there was formation of new metastable martensite in prior austenite grains as a phase change occurred. This behaviour agreed with the equilibrium phase diagram obtained via MatCalc for Eurofer-97. Even after short (4 hour) exposures to 850ºC there is formation of new martensite packets and fully martensitic microstructure in prior austenite grains after 24 hours at 950ºC.

Eurofer-97 was also laser-exposed to mimic the results of thermal finite element modelling of plasma-wall interaction using Comsol Multiphysics. Samples heated repeatedly from 400ºC – 850ºC in 12 seconds showed coarsening of Cr-rich precipitates as well as large, 5 – 40 µm, equiaxial ferrite grains. Coarse Cr-rich precipitates were found to be both intergranular and intragranular. Similar precipitate behaviour was seen in large, ~100 µm, grains seen in the sample aged for 168 hours 800ºC where grain recrystallisation may have occurred.

While the reactor will not see these high temperatures in the continuous condition, it may be subjected to transient exposure similar to that considered in this study. Significant microstructural changes have been observed in Eurofer-97 after 168 hours at a range of temperatures as well as from the result of a pulsed laser exposure to mimic more realistically the effects of repeated thermal transients. These changes could affect the material properties in terms of ductility, creep behaviour, and corrosion resistance and therefore are important in the consideration of fusion plant design and operation.

6.2 Scope for Further Work

Further work on this topic could explore the effects of plasma-wall interactions on oxide-dispersed variants of Eurofer-97, and the tungsten-Eurofer-97 joint where the maximum Eurofer-97 temperatures will be reached. Additionally, the combined effects of plasma-wall interactions with other fusion environment phenomena as high fluxes of 14.1 MeV fusion neutrons, tritium absorption and retention, and magnetic fields should be studied.

Commented [DK11]: After PF comments chat: is there a place for this in the conclusion?

Declarations of Competing Interest

The authors declare that they have no known competing financial interests or personal relationships that could have appeared to influence the work reported in this paper.

Acknowledgements

The authors would like to thank UKAEA/CCFE for the provision of a representative specimen of Eurofer-97. D. Kumar would like to thank EPSRC and NNL for the funding of his doctoral training partnership PhD project, and J. Hargreaves would like to thank the Centre for Doctoral Training in Nuclear Energy Futures for funding his PhD (UK EPSRC grant EP/S023844/1). Dr James Smith and Mr Gary Wan are thanked for their assistance with the laser apparatus.

References

[1] M. Abdou *et al.*, "Blanket/first wall challenges and required R&D on the pathway to DEMO," *Fusion Engineering and Design*. 2015.

[2] L. Giancarli *et al.*, "Test blanket modules in ITER: An overview on proposed designs and required DEMO-relevant materials," *J. Nucl. Mater.*, vol. 367–370, pp. 1271–1280, Aug. 2007.

[3] F. Romanelli *et al.*, "Fusion Electricity: A roadmap to the realisation of fusion energy," *EFDA*, 2012.

[4] H. Bolt *et al.*, "Materials for the plasma-facing components of fusion reactors," *J. Nucl. Mater.*, vol. 329–333, pp. 66–73, Aug. 2004.

[5] R. Aymar, P. Barabaschi, and Y. Shimomura, "The ITER design," *Plasma Phys. Control. Fusion*, vol. 44, pp. 519–565, 2002.

[6] R. Lässer *et al.*, "Structural materials for DEMO: The EU development, strategy, testing and modelling," *Fusion Eng. Des.*, vol. 82, no. 5–14, pp. 511–520, 2007.

[7] Z. Tong and Y. Dai, "The microstructure and tensile properties of ferritic/martensitic steels T91, Eurofer-97 and F82H irradiated up to 20 dpa in STIP-III," *J. Nucl. Mater.*, vol. 398, no. 1–3, pp. 43–48, 2010.

[8] K. Shiba and A. Hishinuma, "Low-temperature irradiation effects on tensile and Charpy properties of low-activation ferritic steels," *J. Nucl. Mater.*, vol. 283–287, no. PART I, pp. 474–477, 2000.

[9] D. R. Harries, G. J. Butterworth, A. Hishinuma, and F. W. Wiffen, "Evaluation of reduced-activation options for fusion materials development," *J. Nucl. Mater.*, vol. 191–194, pp. 92–99, Sep. 1992.

[10] Https://www.iter.org/sci/iterandbeyond, "After ITER," 2019. [Online]. Available: https://www.iter.org/sci/iterandbeyond. [Accessed: 18-Jan-2019].

[11] Y. Poitevin *et al.*, "Progresses and challenges in supporting activities toward a license to operate European TBM systems in ITER," *Fusion Eng. Des.*, vol. 89, no. 7–8, pp. 1113–1118, Oct. 2014.

[12] J. Aubert, G. Aiello, N. Jonquères, A. Li Puma, A. Morin, and G. Rampal, "Development of the water cooled lithium lead blanket for DEMO," *Fusion Eng. Des.*, vol. 89, no. 7–8, pp. 1386–1391, Oct. 2014.

[13] R. Lindau *et al.*, "Present development status of EUROFER and ODS-EUROFER for application in blanket concepts," *Fusion Eng. Des.*, 2005.

[14] A. Del Nevo *et al.*, "WCLL breeding blanket design and integration for DEMO 2015: status and perspectives," *Fusion Eng. Des.*, vol. 124, pp. 682–686, Nov. 2017.

[15] R. Wenninger, R. Albanese, R. Ambrosino, F. Arbeiter, and J. Aubert, "The DEMO wall load challenge," *Nucl. Fusion*, vol. 57, no. 4, pp. 1–11, 2017.

[16] T. N. Todd, “Pulsed DEMO Design Assessment Studies,” *Fusion Sci. Technol.*, vol. 64, no. 2, pp. 76–85, 2013.
[17] P. Domalapally and M. Dellabiancia, “Thermal-hydraulic design of water cooled first wall of the fusion reactor under DEMO conditions,” *Fusion Eng. Des.*, vol. 124, pp. 311–315, Dec. 2017.
[18] Y. Igitkhanov, R. Fetzer, and B. Bazylev, “Effect of heat loads on the plasma facing components of demo,” *Fusion Eng. Des.*, vol. 109–111, pp. 768–772, Dec. 2016.
[19] R. P. Wenninger *et al.*, “DEMO divertor limitations during and in between ELMs,” *Nucl. Fusion*, vol. 54, no. 11, p. 114003, Dec. 2014.
[20] P. Fernández, M. García-Mazarío, A. . Lancha, and J. Lapeña, “Grain boundary microchemistry and metallurgical characterization of Eurofer’97 after simulated service conditions,” *J. Nucl. Mater.*, vol. 329–333, pp. 273–277, Aug. 2004.
[21] P. Fernández, A. . Lancha, J. Lapeña, M. Serrano, and M. Hernández-Mayoral, “Metallurgical properties of reduced activation martensitic steel Eurofer’97 in the as-received condition and after thermal ageing,” *J. Nucl. Mater.*, vol. 307–311, pp. 495–499, Dec. 2002.
[22] W. B. Jones, C. R. Hills, and D. H. Polonis, “Microstructural evolution of modified 9Cr-1Mo steel,” *Metall. Trans. A*, vol. 22, no. 5, pp. 1049–1058, 1991.
[23] Y. De Carlan, A. Alamo, M. H. Mathon, G. Geoffroy, and A. Castaing, “Effect of thermal aging on the microstructure and mechanical properties of 7-11 CrW steels,” *J. Nucl. Mater.*, vol. 283–287, pp. 672–676, 2000.
[24] P. A. Di Maio, P. Arena, G. Bongiovì, P. Chiovaro, A. Del Nevo, and R. Forte, “Numerical assessment of the thermomechanical behaviour of the DEMO Water-Cooled Lithium Lead inboard blanket equatorial module,” *Fusion Eng. Des.*, vol. 136, pp. 1178–1185, Dec. 2018.
[25] F. W. Dittus and L. M. K. Boelter, “Heat transfer in automobile radiators of the tubular type,” *Int. Commun. Heat Mass Transf.*, vol. 12, no. 1, pp. 3–22, 1985.
[26] P. Arena, A. Del Nevo, P. A. Di Maio, R. Forte, and G. Nevone, “Parametric thermal analysis for the optimization of Double Walled Tubes layout in the Water Cooled Lithium Lead inboard blanket of DEMO fusion reactor,” *J. Phys. Conf. Ser.*, vol. 1224, p. 12031, Dec. 2019.
[27] F. Edemetti, E. Martelli, A. Tassone, G. Caruso, and A. Del Nevo, “DEMO WCLL breeding zone cooling system design: Analysis and discussion,” *Fusion Eng. Des.*, vol. 146, pp. 2632–2638, Sep. 2019.
[28] V. Philipps, “Tungsten as material for plasma-facing components in fusion devices,” *J. Nucl. Mater.*, vol. 415, no. 1, Supplement, pp. S2–S9, May 2011.
[29] K. D. Zilnyk, V. B. Oliveira, H. R. Z. Sandim, A. Möslang, and D. Raabe, “Martensitic transformation in Eurofer-97 and ODS-Eurofer steels: A comparative study,” *J. Nucl. Mater.*, vol. 462, pp. 360–367, 2015.
[30] V. B. Oliveira, K. D. Zilnyk, and H. R. Z. Sandim, “Thermodynamic Simulation of Reduced Activation Ferritic–Martensitic Eurofer-97 Steel,” *J. Phase Equilibria Diffus.*, vol. 38, no. 3, pp. 208–216, 2017.
[31] H. Dominguez-Andrade, A. Croot, G. Wan, J. A. Smith, and N. A. Fox, “Characterisation of thermionic emission current with a laser-heated system,” *Rev. Sci. Instrum.*, vol. 90, no. 4, 2019.
[32] S. Nunez-Sanchez, H. D. Andrade, J. Harwood, I. Bickerton, N. A. Fox, and M. J. Cryan, “Molybdenum gratings as a high-temperature refractory platform for plasmonic heat generators in the infrared,” *Micro Nano Lett.*, vol. 13, no. 9, pp. 1325–1328, 2018.
[33] L. I. International, *SPOT Pyrometer User Guide 808273*. Dronfield, U.K., 2018.
[34] A. D. Warren, A. I. Martinez-Ubeda, O. D. Payton, L. Picco, and T. B. Scott,

"Preparation of Stainless Steel Surfaces for Scanning Probe Microscopy," *Micros. Today*, vol. 24, no. 03, pp. 52–55, 2016.

[35] C. Liu, P. J. Heard, O. D. Payton, L. Picco, and P. E. J. Flewitt, "A comparison of two high spatial resolution imaging techniques for determining carbide precipitate type and size in ferritic 9Cr-1Mo steel," *Ultramicroscopy*, vol. 205, no. December 2018, pp. 13–19, 2019.

[36] S. Kano *et al.*, "Instability of MX and M23C6 type precipitates in F82H steels under 2.8 MeV Fe2+ irradiation at 673 K," *Nucl. Mater. Energy*, vol. 17, no. November 2017, pp. 56–61, 2018.

[37] S. Kano *et al.*, "Study of radiation-induced amorphization of M23C6 in RAFM steels under iron irradiations," *J. Nucl. Mater.*, vol. 533, p. 152088, 2020.

[38] J. Chen, K. Yoon, and S.-T. Tu, "Creep Behavior of Pressurized Tank Composed of Functionally Graded Materials," *J. Press. Vessel Technol.*, vol. 133, no. 5, Jul. 2011.